Sound & Vibration 2026, 60(5), 4336.
doi: https://doi.org/10.59400/sv4336

Article

Comparative analysis of simulation explosive methods in coupling charge

Tao Yin[1,*], Fengzhuang Zhang[1], Huayong Guan[1], Ziru Guo[2], Chuanbo Zhou[3], Hongwei Li[2]

[1] School of Civil Engineering and Architecture, Anhui University of Science and Technology, Huainan 232001, China
[2] School of Chemical and Blasting Engineering, Anhui University of Science and Technology, Huainan 232001, China
[3] Faculty of Engineering, China University of Geosciences, Wuhan 430074, China
*** Corresponding author:** Tao Yin, taoyin@aust.edu.cn

CITATION

Yin T, Zhang F, Guan H, et al. Comparative analysis of simulation explosive methods in coupling charge. Sound & Vibration. 2026; 60(5): 4336. https://doi.org/10.59400/sv4336

ARTICLE INFO

Received: 27 April 2026
Revised: 18 June 2026
Accepted: 23 June 2026
Available online: 15 August 2026

Abstract: The accuracy of numerical simulation for blasting behaviors is largely determined by explosive simulation methods. An equivalent amplified explosives method (method 2) for simulating explosives is proposed in this paper. A numerical model for large-diameter low-detonation-velocity explosives is developed to match the same total energy release in rock mass as small-diameter high-detonation-velocity explosives. Compared with existing equivalent methods that apply simplified blast vibration load curves to blast hole walls (method 3) and the plane of center line of blast holes (method 4), the proposed method can accurately characterize the detonation process of explosives and the thermodynamic properties of detonation products. The requirements and characteristics of four different explosive simulation methods are analyzed. Simulations of the blasting of open-pit iron mines were conducted via ANSYS/LS-DYNA, and the simulated vibration velocities obtained were compared with measured velocities. The results showed that field-measured vibration velocities were generally larger than numerical values from all four methods. Specifically, the fluid–structure coupling algorithm (method 1) required the most meshing work and is applicable to few blast holes and near-field analysis. Method 2 is suitable for simulating numerous blast holes and for studying and analyzing the middle and far regions of blast holes. Method 3 is applicable for simulating a few blast holes and for analyzing the middle and far regions of blast holes. Method 4 is also suitable for studying the middle and far regions of the blast holes. These results provide a reference for the numerical simulations of blasting processes under similar conditions.

Keywords: coupling charge; equivalent amplified explosive; explosive simulation; blast load; vibration attenuation law

1. Introduction

The vibrations caused by an explosion may endanger the safe operation of neighboring buildings. When studying the attenuation characteristics of the blasting vibration intensity, vibration tests at the blasting site, small-scale blasting experiments, and numerical simulations are primarily employed. Due to the high temperatures, pressures, and speeds involved in blasting, numerical simulation offers an alternative method for studying blasting processes with the advantages of low cost and high efficiency. Many scientists have studied the simulation of explosives and explosive loads in various blasting processes. For instance, the MAT_HIGH_EXPLOSIVE_BURN explosive material model in LS-DYNA and the corresponding equation of state have been employed to simulate the entire detonation process and the interaction between the detonation products and the surrounding rock [1]. Shin et al. [2] simulated the impact on an adjacent tunnel by modifying field blasting vibration test data and applying it to the outer boundary of the plastic zone around the blast hole. Swoboda and Zenz [3] applied an equivalent blasting load to the blast hole wall. They studied the changes in the plastic zone in the near and far regions from the tunnel face, and the results were compared with those under a static load.

Lu et al. [4] proposed an equivalent simulation method for blasting loads and compared the results with field monitoring data. This method is suitable for predicting the dynamic response of the ground in the far field. Meanwhile, Weng et al. [5] used the strain energy density, an energy index, to simulate the characteristics of energy accumulation and dissipation during rock burst failure. Lu et al. [6] used an equivalent simulation method to model the blasting load and the transient release of in-situ stress, as well as their coupled effects, followed by comparing the simulation results with field monitoring data. Wu et al. [7] proposed a four-step excavation method involving the creation of a vibration-cushioning rock layer in subsequent tunnels adjacent to the existing tunnel. Through numerical simulation, the loss prevention mechanism of the rock layer was modelled and a better understanding of crack propagation in the interlayer rock was achieved. Meanwhile, the effects of confining pressure and discontinuity on the dynamic response and damage mechanism of rock masses were investigated. Jiang et al. [8] used the dynamic finite element method to create a series of numerical models and the Riedel–Hiersiemer–Thoma model to simulate the rock damage caused by explosions. Using isentropic and adiabatic expansion models based on calculations of the blast hole pressure, Chen et al. [9] proposed an improved method for calculating the explosion peak pressure on blast hole walls using uncoupled charges. Similarly, Chen et al. [10] applied a triangular load to a blast hole wall to equivalently simulate an explosion load. Mobaraki et al. [11] investigated the dynamic responses of tunnels buried at depths of 3.5 m, 7 m, 10.5 m, and 14 m in sandy soil under a 1,000 kg TNT surface explosion. Using the finite element software LS-DYNA, the blast resistance of the Kobe box-shaped subway tunnel was evaluated and compared with that of semi-elliptical, circular and horseshoe-shaped tunnels. The results indicated that circular and horseshoe-shaped tunnels exhibited inferior blast resistance compared to the box-shaped tunnel, while the semi-elliptical tunnel demonstrated superior blast resistance.

To reveal the surrounding rock damage characteristics under different excavation schemes, Hu et al. [12] developed a secondary development of the dynamic finite element software LS-DYNA to explore the progressive damage processes of rock masses under smooth blasting and pre-split blasting conditions. To investigate the influence of charge length on blasting vibration, Gou et al. [13] arranged four monitoring points to measure vibration velocities under six different charge lengths. They subsequently performed theoretical calculations of blasting vibrations induced by the superposition of short explosive charges and compared these results with the measured waveforms. They also examined the effects of charge length, detonation position and detonation velocity on the blasting vibrations, concluding that the influence of charge column length on vibration amplitude is significantly dependent on the Mach wave. For a given charge column weight, a greater aspect ratio of the charge column corresponds to a lower vibration amplitude. Huo et al. [14] conducted field raise blasting experiments adopting vertical, parallel and densely clustered long boreholes at the Shaxi underground mine in China. The parameters of the raise outline and the blasting vibrations were measured on-site, with regression analysis subsequently performed for peak particle acceleration (PPA). They established and calibrated a numerical model that considers in-situ stress influences to simulate the excavation process during raise blasting. Jiang et al. [15] adopted the dynamic finite element method to simulate the blasting process in fractured rock masses, thereby revealing the propagation characteristics of blasting stress waves, the evolution patterns of effective stress, and the mechanism underlying damage evolution around boreholes. Based on the Weibull distribution, a rock damage model was developed, and the stress-strain relationship and damage equation for rocks under uniaxial impact loading were derived. The damage equation parameters were calibrated via numerical Split Hopkinson Pressure Bar (SHPB) tests. Jiang et al. [16] investigated the vibration attenuation characteristics of open-pit mine slopes during underground blast mining, taking the Daye Iron Mine as a case study. The dynamic finite element method was first adopted to analyze the characteristics of blasting loads. A three-dimensional numerical model was then constructed to simulate the response of the open-pit mine affected by underground mining activities. Its validity was validated through comparison with on-site monitoring data. The acquired blasting load data were then incorporated into the numerical model for calculating and analyzing PPV distribution laws. Lyu et al. [17] investigated the damage characteristics of grouted surrounding rock under tunnel blasting. Ultrasonic testing was carried out in the tunnel after blasting to determine the acoustic velocity variation pattern of the grouted surrounding rock at various test hole depths. A stress criterion-based statistical damage constitutive model for rock masses was integrated into the dynamic finite element program LS-DYNA to evaluate the surrounding rock damage under cyclic tunnel excavation and blasting.

Cao et al. [18] developed a mathematical-physical method for two-dimensional circular excavations. This method quantifies the relationship between vibration characteristics and various influencing factors, including initial stress, tunnel cross-sectional area, unloading rate and unloading path. The study systematically examined the unloading waveform characteristics under high initial stress conditions, considering different horizontal-to-vertical geostress ratios and rectangular tunnel aspect ratios. Lu et al. [19] developed a coupled model integrating tensile damage and the Drucker-Prager yield criterion to investigate the spatial distribution of blasting-induced damage in the final slope of open-pit mines. The model was validated and analysed using field monitoring data collected from the Wushan Copper Mine. Research findings show that the slope damage severity decreases with increasing burial depth, presenting a nonlinear distribution behind the slope surface. Rehman et al. [20] constructed a three-dimensional finite element model of an underground tunnel via LS-DYNA software, investigating the dynamic response and damage to pre-existing concrete tunnels caused by new tunnel blasting excavation. The results revealed that low-frequency blasting loads are more destructive than high-frequency ones. Moreover, the blast wave frequency significantly affects crack locations in tunnels, primarily inducing cracks at the arch feet and tunnel sidewalls. Xu et al. [21] developed a novel elastoplastic damage constitutive model by integrating the inclusion characteristic time criterion with the unified strength theory. This model captured the increase in dynamic strength throughout the history of equivalent stress. The proposed constitutive model was formulated and numerically implemented based on the non-associated plastic flow rule, the plastic damage evolution law and the equation of state. Guan et al. [22] studied the effects of blasting vibrations on temporary support structures during tunnel construction. First, based on field monitoring data, the dynamic response characteristics of temporary mid-partition walls under blasting disturbance were analyzed. Second, on-site investigations were carried out to explore the damage features of such partition walls near the blasting sources. Subsequently, the finite element software LS-DYNA was employed to simulate the vibration responses and failure modes of the walls under varying charge weights and blasting distances. Huo et al. [23] investigated the failure modes and damage evaluation of underground reinforced concrete arch structures under overhead explosion loads. The dynamic response characteristics of structures at different explosion distances and with various charge masses were systematically tested. A three-dimensional model incorporating rock, concrete and steel reinforcement was established using LS/DYNA software. Gui et al. [24] studied the propagation characteristics of blast waves in rock-soil mixed media and pure rock foundations. The PPVs of monitoring points in horizontal and vertical directions were acquired in their research. The results indicated that the rock-soil interface exerts a substantial influence on blast wave attenuation. Meanwhile, the depth-dependent attenuation effect of PPV was identified in both numerical models.

After reviewing the simulation methods for explosive materials, in the simulation of the explosion load of an explosive, method 3 and method 4 using the Saint Venant principle results in large errors in the near-zone of the blast hole. Since each blasting condition in the near-zone is different, it is impossible to accurately predict the outcome. Therefore, the most common method is to simulate the explosion process using high-energy explosive material models provided by LS-DYNA software. However, the mesh of the blast holes and explosive rolls must be divided into very small sections. This results in abnormal meshes and long calculation times, and it sometimes yields no results from the numerical calculation. It is found that the method 1 is only suitable applicable to cases with a small number of blast holes and near-field analysis. Method 3 still requires a considerable meshing work. This method is suitable for simulating a small number of blast holes and for analyzing the middle and far regions of blast holes. Method 4 involves the lowest meshing work. It is applicable to models with a large number of blastholes, and also works well for analysis of the middle and far regions of the blast holes. To overcome the shortcomings of existing methods, a numerical simulation method of equivalent amplified explosives (method 2) in a coupling charge was proposed in this study. This method accurately describes the explosion state, provides good modelling results, does not produce abnormal grids, and greatly reduces the calculation time.

2. Characteristics of different simulation explosive methods

2.1. Fluid–structure coupling algorithm

For the fluid–solid coupling algorithm, both the explosive and the structure to be blasted were represented by 8-node solid elements. A Eulerian algorithm was used for the fluids (explosives and air), and a Lagrangian algorithm was used for the solids (rock and soil). The fluid–solid coupling algorithm defined a connection between the Eulerian and Lagrangian grid elements to prevent element distortion. The explosion process was simulated using the high-explosive material model MAT_HIGH_EXPLOSIVE_BURN (method 1) provided by the LS-DYNA software.

2.2. Equivalent amplified explosive

When numerically simulating the hazards of seismic waves induced by explosive detonation on adjacent structures, Method 1 is commonly adopted to model the explosion. The diameter of explosive cartridges is several centimeters, while the distance from the charge to the target structures ranges from tens to hundreds of meters, creating a scale difference of 3 to 4 orders of magnitude. Since the cartridge diameter is far smaller than the standoff distance to adjacent structures, extremely fine meshes are required for boreholes and explosive cartridges during numerical modeling. This inevitably leads to distorted meshes, excessive computation time, and even calculation failure. Neither Method 3 nor Method 4 applies loads at both ends of the borehole. In addition, the large equivalent blasting load applied on elements requires relatively coarse meshes to avoid negative element volume, which causes considerable deviations between simulation results and measured data. Moreover, stemming material is not considered in Method 4.

To address the above deficiencies of existing approaches, this paper proposed a numerical simulation method for coupling charges using equivalent amplified explosives (method 2). The method is established on the principle that the stress generated in rock at a distance r from the detonation center is identical for small-diameter high-detonation-velocity explosives and large-diameter low-detonation-velocity explosives. This method includes the following steps (**Figure 1**).

This method includes the following:

(1) A coupling charge of a small-diameter, high-detonation-velocity explosive was selected. A granular ammonium nitrate/fuel oil (ANFO) explosive was used. The radius of the small-diameter, high-detonation-velocity explosive is denoted as r_1, and its detonation velocity is denoted as v_1. Because it was a coupled charge, the radius of the blast hole was $r_c = r_1$. The average detonation pressure (P_1) of the coupling charge of the small-diameter, high-detonation-velocity explosive was calculated by the following formula:

$$P_1 = \frac{\rho_1 {v_1}^2}{2(\gamma + 1)}, \tag{1}$$

where ρ_1 is the density, v_1 is the detonation velocity, and γ is the isentropic index of the small-diameter, high-detonation-velocity explosive. The value of γ was taken as 3, which is suitable for general industrial explosives.

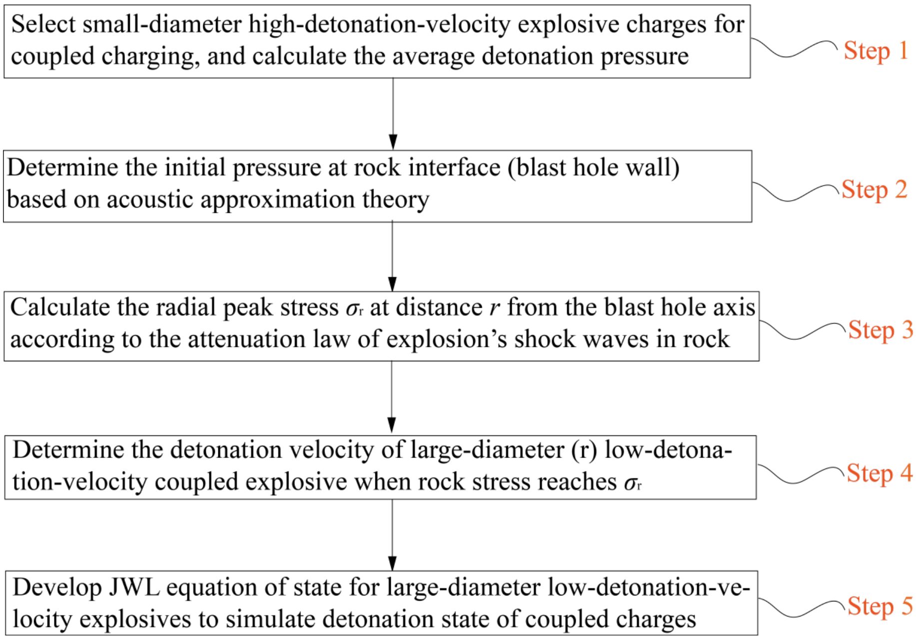

Figure 1. Equivalent amplified explosive flowchart.

(2) According to the acoustic approximation theory, the initial pressure at the rock interface (P_m) was calculated using the following formula:

$$P_m = P_1 \frac{2}{1 + \frac{\rho_1 v_1}{\rho_m v_m}}, \tag{2}$$

where ρ_1 is the density of explosive, v_1 is the detonation velocity of explosive, $\rho_1 v_1$ is the impact impedance of the explosive, ρ_m is the density of rock, v_m is the *P*-wave velocity of rock, $\rho_m v_m$ is the rock wave impedance.

(3) According to the attenuation characteristics of an explosion's shock waves in rock, the wave propagated radially along the blast hole. Due to the continuous compression of the rock medium, the wave velocity decreased and the peak stress attenuated. The radial peak stress (σ_r) at a position (r) from the blast hole axis could be calculated using the following formula:

$$\sigma_r = p_m \left(\frac{r_c}{r}\right)^{\alpha}, \tag{3}$$

where $\alpha = 1.5$ [25], and r_c is the blast hole radius. Due to the coupling charge, the radius of the large-diameter, low-detonation-velocity explosive is r, which was $r_2 = 0.6$ m from the blast hole center. This is the equivalent of an enlarged blast hole radius.

(4) According to the principle of equal explosion energy, a coupling charge of a small-diameter, high-detonation-velocity explosive was equivalent to that of a large-diameter, low-detonation-velocity explosive. The detonation velocity (v_2) of a large-diameter (r_2), low-detonation-velocity explosive was calculated using the following formulas when the stress value (σ_r) in the rock after the explosion was reached:

$$P_2 = \frac{\rho_2 {v_2}^2}{2(\gamma + 1)}, \tag{4}$$

$$P_3 = P_2 \frac{2}{1 + \frac{\rho_2 v_2}{\rho_m v_m}}, \tag{5}$$

$$P_3 = \sigma_r, \tag{6}$$

where P_2 is the average initial detonation pressure of the large-diameter, low-detonation-velocity explosive, ρ_2 is the density of the large-diameter, low-detonation-velocity explosive, v_2 is the detonation velocity of the large-diameter, low-detonation-velocity explosive, P_3 is the initial pressure at the rock interface, and $\rho_2 v_2$ is the impact impedance of the large-diameter, low-detonation-velocity explosive.

Based on the formulas above, the detonation velocity (v_2) of a large-diameter, low-detonation-velocity explosive can be obtained.

(5) The detonation velocity of a large-diameter, low-detonation-velocity explosive, calculated using the formulas above, was used to establish the detonation equation of state of the explosive to simulate the detonation state of the coupling charge explosive. This was based on the Jones–Wilkins–Lee (JWL) equation of state [26]:

$$P = A\left(1 - \frac{\omega}{R_1 V}\right) e^{-R_1 V} + B\left(1 - \frac{\omega}{R_2 V}\right) e^{-R_2 V} + \frac{\omega E_0}{V}, \tag{7}$$

where P is the pressure, A, B, R_1, R_2, and ω are the material constants related to the explosive, V is the relative volume, E_0 is the initial specific internal energy.

V_{CJ} is the explosive capacity of the explosive, and ρ_2 is the density of the explosive. In this study, $A = 5.35545\rho_2 v_2^2$, $B = 0.094983\rho_2 v_2^2$, $R_1 = 4.2$, $R_2 = 0.27R_1 = 1.13$, $\omega = 0.33$, $E_0 = \rho_2 v_2^2\,(0.204 - 0.0734\rho_2)$, $l = \sqrt{\frac{\rho_2 v_2^2}{2E_0} + 1}$, and $V = V_{CJ} = \frac{l}{l+1}$.

Equation (7) can be used for explosives with a large diameters and low detonation velocities using the explosive density (ρ_2) and the detonation velocity (v_2).

2.3. Triangular load applied to blast hole wall

In this method, the simplified blasting vibration load curve was applied directly to the blast hole wall (method 3), without considering the shape of the blast hole during modelling. This reduced the calculation time significantly compared to those required for method 1, but meshing still required a large amount of work.

(1) Peak value of blasting load

The average detonation pressure of the explosive was obtained by Equation (1) under the Chapman–Jouguet (C–J) detonation condition.

The pressure exerted on the blast hole wall was equivalent to the detonation pressure of the explosive for the coupling charge. Then,

$$P_D = P_1, \tag{8}$$

where P_1 is the peak pressure of the blasting load during the coupling charge detonation (Pa), P_D is the pressure exerted on the blast hole wall.

(2) Boosting time (t_r) and positive pressure acting time

Under the blasting load, the boosting time (t_r) and the positive pressure acting time

(t_s) were calculated as follows:

$$t_r = 12\sqrt{r^{2-u}}Q^{0.05}/K, \tag{9}$$

$$t_s = 84\sqrt[3]{r^{2-u}}Q^{0.2}/K, \tag{10}$$

where K is the bulk compression modulus of the rock mass (Pa), μ is the Poisson's ratio of the rock mass, Q is the amount of charge in the blast hole (kg), and r is the ratio of the distance from the charge center to the blast hole radius, which was taken as 1 for a coupling charge. The relationship between the bulk modulus (K), the elastic modulus (E), and the Poisson's ratio (μ) is $K = \frac{E}{3(1-2\mu)}$.

In the simulation analysis, it was necessary to ensure that the defined load time range exceeded the solution time and that the load was defined as zero after the positive pressure action time (t_s). The pressure load needed to be applied to the surface of component elements, such as the three-dimensional Solid 164 element, which had six surfaces. The program needed to be informed of which surface was being loaded during the loading process. When blasting with a cylindrical charge, consideration needed to be given to the propagation process of the detonation wave. The cylindrical explosive needed to be divided into multiple elements. The more elements were included, the more accurate the simulation results became. To balance the calculation time and simulation accuracy, the grain was divided into n elements, the explosive height was h, and the initiation delay ($t = \frac{h}{nv}$) for each element was determined by the detonation wave propagation velocity (v). After the initiation delay time (t), the same blasting load was applied to the element of the blast hole wall. The initiation time of the first element at the bottom of the hole was set to 0, and the initiation times of the other elements from the bottom of the hole to the orifice were set to t, $2t$, …, $(n-1)t$. The thickness of the rock element of the blast hole wall was set to 6 cm to prevent it from being pressed through when the load was applied, which would result in negative volumes.

2.4. Triangular load applied to plane of center line of blast holes

In this method, a simplified triangular pulse load was applied to the plane defined by the center line connecting the holes in the same row and the axis of the holes (method 4). There were no blast holes in the model, which reduced the meshing workload. The number of elements was also greatly reduced, and the time taken for the computer calculations was significantly shorter.

It was assumed that there was a pressure (P_0) acting on the wall of a single blast hole. The radius of each blast hole was r_0, and the hole spacing was a. The same row of blast holes was arranged into a vertical plane, and the equivalent pressure to be applied on the center line of the blast holes was

$$P_e = (2r_0/a)P_0. \tag{11}$$

For three-dimensional problems, the equivalent pressure was applied to the plane defined by the blast hole axis and the center line of the row of blast holes. The depth range of the pressure was equal to the length of the charge section in the blast hole.

Similarly, the initiation times of the elements were the same as those in method 3. The distance between the rocks under pressure was 20 cm, and the thickness of the rock under pressure was 10 cm to avoid negative volumes of the rock elements.

2.5. Comparative analysis of four methods

The key parameters (with units), applicable scopes and limitations of all four simulation methods were systematically listed, as presented in **Table 1**.

Table 1. Comparative analysis of four methods.

Methods for simulation of explosive blast loads	Method 1	Method 2	Method 3	Method 4
Key parameters	Detonation velocity (m/s), C-J detonation pressure (Pa), JWL equation coefficients (R_1, R_2, A, B, ω), detonation energy per unit volume ($\mathrm{J/m^3}$), initial relative volume	Detonation velocity (m/s), C-J detonation pressure (Pa), JWL equation coefficients (R_1, R_2, A, B, ω), detonation energy per unit volume ($\mathrm{J/m^3}$), initial relative volume	Peak value of blasting load (Pa), boosting time (μs) and positive pressure acting time (μs)	Peak value of blasting load (Pa), boosting time (μs) and positive pressure acting time (μs)
Applicable conditions	Applicable to few blastholes and near-field analysis	Applicable to abundant blastholes and mid-far field	Applicable to abundant blastholes and mid-far field	Applicable to abundant blastholes and mid-far field
Limitations	Required the most meshing work and not applicable to the middle and far regions of blast holes	Not applicable to near-field analysis	Required plenty of meshing work, not applicable to near-field analysis	Required the least meshing work, not applicable to near-field analysis

3. Numerical simulation model of open-pit bench blasting

The open-pit bench blasting process was simulated using the ANSYS/LS-DYNA dynamic finite element software to analyze the feasibility of the proposed numerical simulation method for equivalent amplified explosives in a coupling charge. The predictions were then compared with measured vibration velocity data and the predictions of three other methods.

3.1. Engineering and geological characteristics of open-pit iron ore mine

The ore mine extended 3 km from south to north and 1.5 km from east to west. The ore minerals were mainly lean hematite ore, followed by hematite. Most of the rocks were migmatite. The Presinian strata contained biotite granulite and the particles consisted of relatively slender gneiss, schist, and magnetite quartz sandstone. The rocks in the Sinian strata included biotite granulite, pegmatite, and quartz sandstone, and the top layer consisted of gravel, clay, sandy soil, and sand [27].

The blasting parameters were as follows: a mixed ANFO explosive, an electronic digital detonator, a vertical deep hole, blast hole diameter of 28 cm, a powdered Ammonium Nitrate Fuel Oil (ANFO) explosive coupling charge, a hole depth of 17 m, a charge height of 13 m, a filling height of 4 m, a hole spacing of 5 m, and a distance from the bench slope of 5 m. After loading the explosives, the blast hole was blocked with crushed stones. TC-4850N blasting vibration meters (manufactured by Chengdu Zhongke Measurement and Control Co., Ltd.) were used to test the blasting vibration data at three observation points: 15, 25, and 45 m from a single blast hole. The blast hole layout was shown in **Figure 2**.

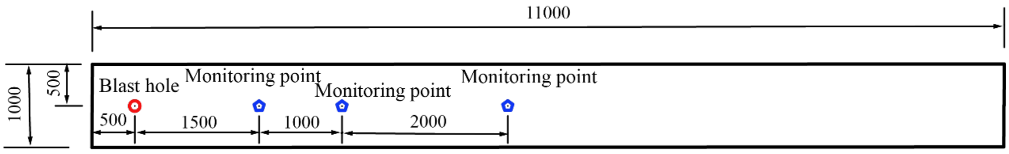

Figure 2. Blast hole layout (cm).

3.2. Calculation model and parameters

The vibration effect of an open-air blasting bench during the explosion of an explosive was simulated using the dynamic finite element software ANSYS/LS-DYNA. The research project focused on a blasthole, and to reduce the computational workload, a half-model was constructed, as illustrated in **Figure 3**. The numerical model dimensions were 11,000 × 500 × 2,500 cm (X direction × Y direction × Z direction), and the mesh was divided using three-dimensional solid 164 elements. The rock and stemming materials were modelled using a Lagrangian grid, while the explosives and air were established using a Eulerian grid. A fluid–structure coupling algorithm was utilized to establish the connection between these elements. The cm-g-μs unit system was adopted.

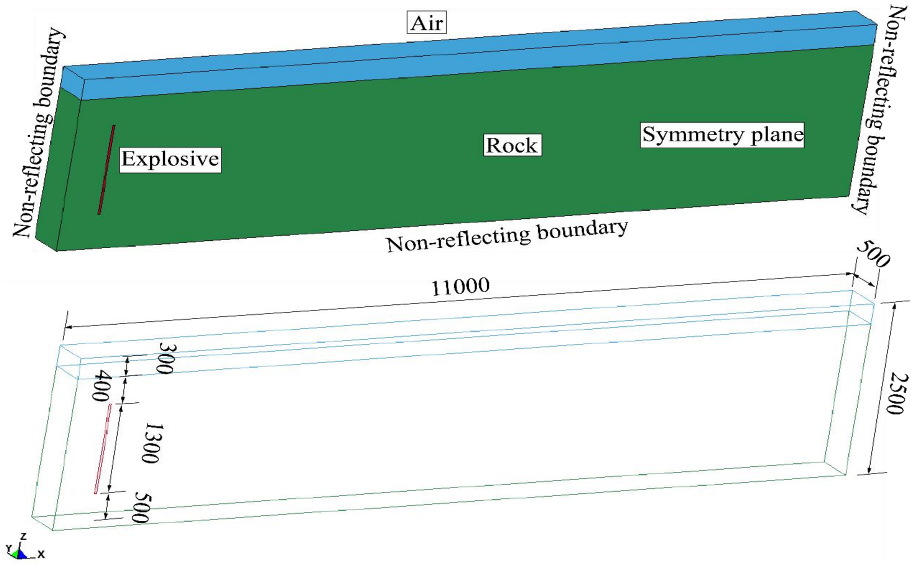

Figure 3. Calculation model for open-air bench blasting.

(1) Explosive material model

The explosives were modelled using the built-in high-energy explosive material model MAT_HIGH_EXPLOSIVE_BURN in LS-DYNA, with the JWL equation of state, given in Equation (7). The parameters of the explosives and the JWL equation are listed in **Table 2**.

Table 2. Explosive materials and equation of state parameters.

Density/(g/cm^3)	Explosion velocity/(m/s)	A/GPa	B/GPa	R_1	R_2	ω	E/GPa
1.0	3,230	323.8	0.19	4.3	0.8	0.15	3.51

(2) Constitutive model of rock mass material and stemming material

Both the rock mass and the stemming material were modelled using the

MAT_PLASTIC_KINEMATIC elastoplastic dynamic model. The parameters for both are listed in **Table 3**.

Table 3. Rock and stemming material parameters.

Density/(g/cm^3)	Modulus of elasticity/GPa	Poisson's ratio	Yield stress (10^{11}Pa)	Tangent modulus/GPa	Hardening parameter	Strain rate parameter
2.35	56.6	0.24	3.0e-5	5.4	1.0	0.06

(3) Air material

The air was modelled with the MAT_NULL material model and the EOS_LINEAR_POLYNOMIAL equation of state, which is shown as follows:

$$P = \frac{\rho_0 c^2 \mu \left[1 + \left(1 - \frac{\gamma_0}{2}\right)\mu - \frac{\alpha}{2}\mu^2\right]}{\left[1 - (S_1 - 1)\mu - S_2 \frac{\mu^2}{\mu+1} - S_3 \frac{\mu^3}{(\mu+1)^2}\right]} + (\gamma_0 + \alpha\mu) e_0, \tag{12}$$

where P denotes the pressure, ρ_0 denotes the initial density of the material, ρ denotes the density of the material, $\mu = \frac{\rho}{\rho_0} - 1$, C denotes the intercept of the shear-compression wave speed curve, S_1, S_2, and S_3 denote the slope factors of the shear-compression wave speed curve, γ_0 denotes the Grüneisen constant, α denotes the initial volume correction factor, and e_0 denotes the initial specific internal energy. The air material parameters are presented in **Table 4**.

Table 4. Air material parameters.

ρ_0 (g·cm^{-3})	C (m·s^{-1})	S_1	S_2	S_3	γ_0	α	e_0(GPa)
1.29×10^{-3}	344	0	0	0	1.40	0	0

3.3. Mesh convergence analysis

Kuhlemeyer and Lysmer [28] suggested that the mesh size should be less than 1/8–1/10 of the wavelength. Given the *P*-wave velocity of 4,700 m/s and the dominant frequency ranging from 5 to 100 Hz obtained from field monitoring, the maximum element size was determined to be 4.7 m, however, an excessively fine mesh would lead to a substantial increase in computational time. Considering the above factors comprehensively, the maximum element size was set to 0.5 m. The grid independence of the other three methods had been discussed by Lu et al. [4]. This study conducted a grid convergence analysis for the newly proposed method 2. All geometric dimensions, material parameters, loads, boundary conditions and solution settings of the model were kept identical, while only the element size was varied as 0.5 m, 0.25 m and 0.17 m. For the three mesh schemes, the PPV was extracted at the node located 5,250 cm in the X-direction, 0 cm in the Y-direction and 1,300 cm in the Z-direction from the detonation source. The comparison results were presented in **Table 5**.

Table 5. PPVs for three element sizes.

Element size (m)	PPV at the same node (cm/s)
0.5	0.126
0.25	0.131
0.17	0.128

Comparison of PPV results from the three meshes shows that the relative error between two adjacent sets of data is below 4% at the element size of 0.5 m, which meets the mesh convergence criterion. Balancing computation time and precision, the 0.5 m element size is used for further calculations.

4. Comparative analysis of vibration attenuation characteristics of open-air bench blasting

A comparative analysis between the results of four simulation methods and measured data was conducted, focusing on three aspects: the simulation process, the attenuation characteristics of the PPV with distance from the explosion center, and the number of nodes and elements in the models.

4.1. Comparison of simulation processes using four methods

In method 1, when simulating the explosion of explosives and the subsequent seismic waves generated by the explosion, which may result in damage to nearby buildings and structures, the diameter of the explosive charge was several centimeters. In contrast, the distance between a building or structure and the explosive would be tens to hundreds of meters. This represents a difference of 3 to 4 orders of magnitude. Therefore, the diameter of the explosive charge was comparatively diminutive in relation to the distance to a proximate building or structure. In the context of numerical modelling, the grid for the blasthole and explosive charge must be meticulously refined, a process that can give rise to a number of issues. These include distorted grids, protracted calculation times, and the failure to obtain results during numerical calculations.

Method 2 can accurately describe the explosion state, provides a good modelling effect, and does not produce abnormal grids. It can also significantly reduce the calculation time. In method 3, no load was applied to the top or bottom of the blast hole. When a load was applied, the element was pressed through, resulting in a negative volume. To address this, the grid also needed to be relatively large when the load was applied. In method 4, to prevent a negative volume of elements, the grid needed to be divided into larger sections. No loads were applied to the top or bottom of the blast hole.

4.2. Attenuation laws of peak particle velocities under four methods

The attenuation laws of peak particle velocities under the four methods are shown in **Table 6** and **Figure 4**.

Table 6. Attenuation law of peak particle velocities (PPVs).

Distance from explosion source/(m)	10	15	20	25	30	35	40	45	50	55
Measured PPVs/(cm/s)		30.2		17.9				9.83		
Method 1/(cm/s)	1.68	2.96	1.80	1.38	1.11	1.22	1.57	2.49	0.89	2.68
Method 2/(cm/s)	6.49	16.31	14.05	5.0	4.13	7.06	6.12	5.41	8.50	6.27
Method 3/(cm/s)	2.33	3.73	2.93	1.67	2.00	2.24	0.72	3.06	0.84	1.19
Method 4/(cm/s)	7.06	6.12	7.09	3.11	4.10	3.05	4.01	3.15	4.0	3.10

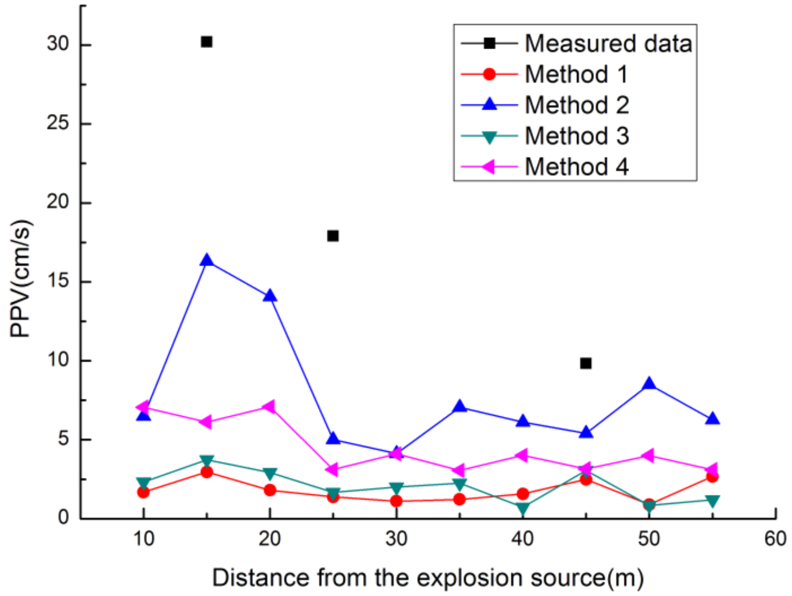

Figure 4. Attenuation of peak particle velocities (PPVs).

As can be seen in **Figure 4**, the PPVs predicted by the four methods were all smaller than the measured PPVs. The discrepancies between numerical predictions and field measurements originate from the complexity of in-situ geological conditions, simplification of the constitutive model, and idealization of construction working conditions. The superposition of blast-induced seismic waves leads to either constructive amplification or destructive cancellation of vibration signals, resulting in minor local fluctuations in measured PPV values. In the near-blasthole area, the simulation results for methods 1 and 3 differed significantly from the measured data, whereas the difference was smaller for method 4 and the smallest for method 2. In the far-blasthole area, the PPVs predicted by the four methods were all close to the measured PPV.

4.3. PPV attenuation curves of four methods

The PPV attenuation curves of four methods are shown in **Figure 5**.

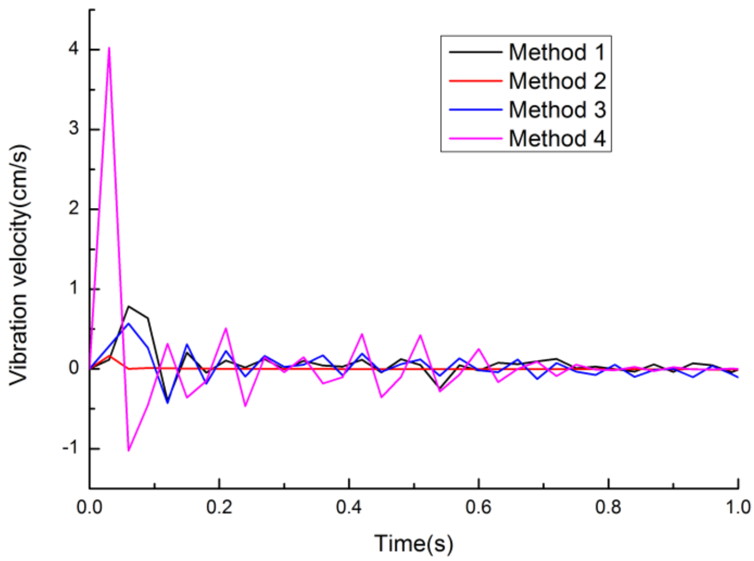

(a) X direction.

Figure 5. *Cont.*

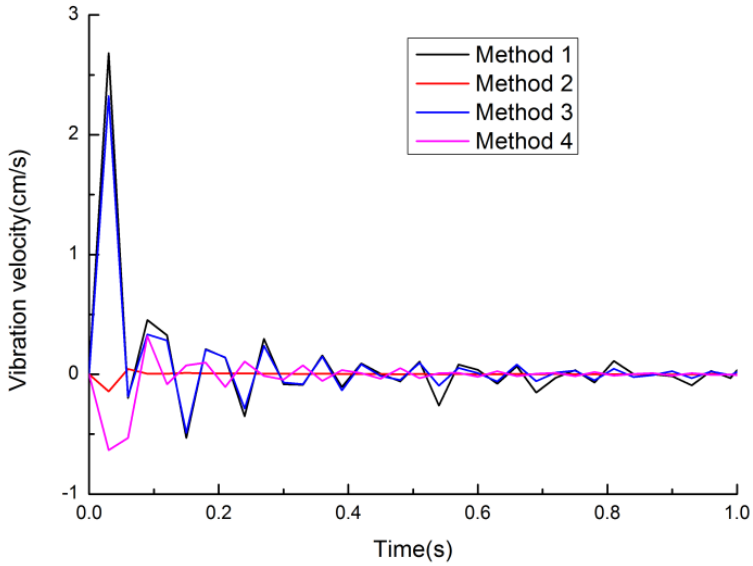

(b) Z direction.

Figure 5. PPV attenuation curves of four methods.

It can be seen from **Figure 5** that the vibration periods calculated by the four simulation methods are basically consistent. In the X-direction, method 4 has the maximum PPV, method 3 ranks the second, method 1 the third, and method 2 the minimum. In the Z direction, method 1 has the highest PPV, method 3 ranks second, method 1 third, and method 2 the lowest. The occurrence time of PPV is nearly identical for all four methods, and the waveforms show similar evolution characteristics across all four methods.

4.4. Number of nodes and elements of model for four methods

The number of nodes and elements of model for four methods are shown in **Table 7**.

Table 7. Number of nodes and elements of the model.

	Method 1	**Method 2**	**Method 3**	**Method 4**
Number of nodes	124,797	123,981	124,160	123,756
Number of elements	110,800	110,000	110,098	109,740
Number of small elements	100	0	96	0

As shown in **Table 7**, the numerical simulations conducted under equivalent operating conditions required 124,797 nodes in method 1; 123,981 nodes in method 2; 124,160 nodes in method 3; and 123,756 nodes in method 4. Method 1 had the highest number of nodes, while method 4 had the lowest. Method 2 exhibited a reduction of 816 nodes compared to the number in method 1, representing a 0.65% decrease. Similarly, method 3 demonstrated a reduction of 637 nodes compared to the number in method 1, also corresponding to a 0.51% decrease. Method 4 showed a reduction of 1,041 nodes compared to the number in method 1, also corresponding to a 0.83% decrease.

The numbers of elements required in Methods 1, 2, 3, and 4 were 110,800, 110,000, 110,098, and 109,740, respectively. Method 1 had the highest number of elements, while method 4 had the lowest. The number of elements in method 2 was 800 fewer than that in method 1, representing a decrease of 0.72%. The number of elements in method 3 was 702 fewer than that in method 1, representing a decrease of 0.63%. The number of elements in method 4 was 1,060 fewer than that in method 1, representing a decrease of 0.96%.

In method 1, there were 100 small elements, including 52 explosive elements, 12 air elements, 16 rock elements, and 20 stemming material elements. There were no small elements in method 2. In method 3, there were 96 elements, including 24 air elements, 32 rock elements, and 40 stemming material elements, but no explosive elements. There were no small elements in method 4, and the explosive elements were also omitted.

4.5. Computation time comparison of the four methods

The geometric dimensions, material properties, applied loads, mesh sizes, boundary conditions and solver parameters of the model were kept consistent across all cases. The computation time comparison of the four methods is presented in **Table 8**.

Table 8. Computation time comparison of the four methods.

	Method 1	**Method 2**	**Method 3**	**Method 4**
Computation time	1 h 3 min 28 s	33 min 59 s	3 h 14 min 34 s	1 h 1 min 50 s

As shown in **Table 8**, method 2 yields the minimum computation time (33 min 59 s), followed by method 4 (1 h 1 min 50 s) and method 1. Method 3 takes the longest time. Relative to method 1, method 2 and method 4 reduce computation time by 46.45% and 2.57% respectively, while method 3 increases it by 206.57%.

5. Conclusion

In this study, although the PPVs predicted by the four simulation methods were smaller than those of the actual test, the differences were not significant. Method 1 is suitable for simulating a small number of blast holes and for studying and analyzing the areas near the blast holes. In contrast to traditional methods, method 2 produces a good model, does not generate abnormal grids, and can significantly reduce the calculation time. It is suitable for simulating a large number of blast holes and for studying and analyzing the middle and far regions of blast holes. However, dividing the mesh for method 3 still requires a significant amount of work, which is suitable for simulating a small number of blast holes and for studying and analyzing the middle and far regions of blast holes. However, method 4 requires minimal meshing work. Thus, this method suitable for simulating a large number of blast holes and for studying and analyzing the middle and far regions of the blast holes.

Author contributions: Conceptualization, ZG and CZ; methodology, HL; software, TY; validation, FZ and HG; formal analysis, FZ; investigation, FZ; resources, CZ; data curation, HG; writing—original draft preparation, TY; writing—review and editing, TY; visualization, TY; supervision, TY; project administration, TY; funding acquisition, TY. All authors have read and agreed to the published version of the manuscript.

Funding: The research was sponsored by the Anhui Engineering Laboratory of Explosive Materials and Technology, Anhui University of Science and Technology (grant No. AHBP2022B-05).

Institutional review board statement: Not applicable. The present work only adopts numerical simulation method to analyze open-pit coupled charge blasting responses of rock mass, and no human trials, animal experiments or biological sample tests are carried out in the whole research. Therefore, ethical review approval is not required for this study.

Informed consent statement: Not applicable. This paper only carries out numerical simulation analysis of open-pit coupled charge blasting engineering based on LS-DYNA software, and no human subjects or human-related experiments are involved in the whole research process.

Data availability statement: The raw numerical calculation files, model parameters and output data generated by the LS-DYNA simulation in this study are preserved in the laboratory server of the research group. The datasets are not publicly available due to the constraints of laboratory data management rules. Reasonable data requests for academic research can be submitted to the corresponding author upon valid application.

Acknowledgment: We thank LetPub (www.letpub.com.cn) for its linguistic assistance during the preparation of this manuscript.

Conflict of interest: The authors declare no conflict of interest.

AI use statement: During the preparation of this manuscript, the authors used Doubao solely for language refinement. No AI tools were used for data analysis, interpretation, or generation of scientific content. All outputs were critically reviewed and edited by the authors. The authors take full responsibility for the integrity and accuracy of the work.

References

1. Livermore Software Technology Corporation. LS-DYNA Keyword User’s Manual. LSTC Co; 2007.
2. Shin JH, Moon HG, Chae SE. Effect of blast-induced vibration on existing tunnels in soft rocks. Tunnelling and Underground Space Technology. 2011; 26(1): 51–61.
3. Swoboda G, Zenz G. Practical considerations of blast loading in tunneling using numerical modeling. In: Proceedings of the Sixth International Conference on Numerical Methods in Geomechanics; 11–15 April 1988; Innsbruck, Austria.
4. Lu W, Yang J, Chen M, et al. An equivalent method for blasting vibration simulation. Simulation Modelling Practice and Theory. 2011; 19(9): 2050–2062.
5. Weng L, Huang L, Taheri A, et al. Rockburst characteristics and numerical simulation based on a strain energy density index: A case study of a roadway in Linglong gold mine, China. Tunnelling and Underground Space Technology. 2017; 69: 223–232.
6. Lu W, Yang J, Yan P, et al. Dynamic response of rock mass induced by the transient release of in-situ stress. International Journal of Rock Mechanics and Mining Sciences. 2012; 53: 129–141.
7. Wu X, Gong M, Wu H, et al. Vibration reduction technology and the mechanisms of surrounding rock damage from blasting in neighborhood tunnels with small clearance. International Journal of Mining Science and Technology. 2023; 33(5): 625–637.

8. Jiang X, Xue Y, Kong F, et al. Dynamic responses and damage mechanism of rock with discontinuity subjected to confining stresses and blasting loads. International Journal of Impact Engineering. 2023; 172: 104404.
9. Chen M, Ye Z, Lu W, et al. An improved method for calculating the peak explosion pressure on the borehole wall in decoupling charge blasting. International Journal of Impact Engineering. 2020; 146: 103695.
10. Chen S, Zhao J, Zhou Y. UDEC modeling of a field explosion test. Fragblast. 2000; 4(2): 149–163.
11. Mobaraki B, Vaghefi M. Numerical study of the depth and cross-sectional shape of tunnel under surface explosion. Tunnelling and Underground Space Technology Incorporating Trenchless Technology Research. 2015; 47: 114–122.
12. Hu Y, Lu W, Chen M, et al. Comparison of Blast-Induced Damage Between Presplit and Smooth Blasting of High Rock Slope. Rock Mechanics & Rock Engineering. 2014; 47(4): 1307–1320.
13. Gou Y, Ye M, Yu Z, et al. Experimental and theoretical analysis of charge length on single-hole vibration amplitude from underground deep-hole blasting. International Journal of Rock Mechanics and Mining Sciences. 2024; 182: 105876.
14. Huo X, Shi X, Qiu X, et al. A study on raise blasting and blast-induced vibrations in highly stressed rock masses. Tunnelling and Underground Space Technology. 2022; 123: 104407.
15. Jiang X, Xue Y, Ren X, et al. Dynamic response characteristics and damage calculation method of fractured rock mass under blasting disturbance. International Journal of Impact Engineering. 2024; 192: 105036.
16. Jiang N, Zhou C, Lu S, et al. Propagation and prediction of blasting vibration on slope in an open pit during underground mining. Tunnelling and Underground Space Technology. 2017; 70: 409–421.
17. Lyu G, Zhou C, Jiang N. Experimental and Numerical Study on Tunnel Blasting Induced Damage Characteristics of Grouted Surrounding Rock in Fault Zones. Rock Mechanics and Rock Engineering. 2023; 56(1): 603–617.
18. Cao W, Li X, Tao M, et al. Vibrations induced by high initial stress release during underground excavations. Tunnelling and Underground Space Technology. 2016; 53: 78–95.
19. Lu Y, Jin C, Wang Q, et al. Numerical study on spatial distribution of blast-induced damage zone in open-pit slope. International Journal of Rock Mechanics and Mining Sciences. 2023; 163: 105328.
20. Rehman JU, Park D, Ahn JK. Predicting Blast-Induced Damage and Dynamic Response of Drill-and-Blast Tunnel Using Three-Dimensional Finite Element Analysis. Applied Sciences. 2024; 14(14): 6152.
21. Xu X, Chi LY, Chen YPW. An elastoplastic damage constitutive model for capturing dynamic enhancement effect of rock and concrete through equivalent stress history. International Journal of Impact Engineering. 2023; 181: 104736.
22. Guan X, Yang N, Zhang W, et al. Vibration response and failure modes analysis of the temporary support structure under blasting excavation of tunnels. Engineering Failure Analysis. 2022; 136: 106188.
23. Huo Q, Liu G, Wang W, et al. Failure mode and damage assessment of underground reinforced concrete arched structure under side top explosion. Structures. 2024; 59: 105801.
24. Gui YL, Zhao ZY, Jayasinghe LB, et al. Blast wave induced spatial variation of ground vibration considering field geological conditions. International Journal of Rock Mechanics and Mining Sciences. 2018; 101: 63–68.
25. Henrych J. The Dynamics of Explosion and Its Use. Elsevier Scientific Publishing Company; 1979.
26. Souers P, Haselman Jr L. Detonation Equation of State at LLNL, 1993. Lawrence Livermore National Laboratory (LLNL); 1994.
27. Zhou M, Zhang YP, Cui JY, et al. Numerical Simulation on Offset of Seismic Wave Peaks and Valleys in Deep-hole Blasting. Journal of North China University of Science and Technology (Natural Science Edition). 2022; 44(1): 10. (in Chinese)
28. Kuhlemeyer RL, Lysmer J. Finite element method accuracy for wave propagation problems. Journal of the Soil Mechanics and Foundations Division. 1973; 99(5): 421–427.